Xiao-Han Gong, Ji-Feng Xu, Ren-Deng Shi, Ben-Xun Su, Qi-Shuai Huang, and Xiao-Xiao Huang, 2021, Subduction initiation-induced rapid emplacement of garnet-bearing peridotites at a nascent forearc: Petrological and Os-Li isotopic evidence from the Purang ophiolite, Tibet: GSA Bulletin, https://doi.org/10.1130/B35960.1.

Supplemental Material

Supplemental Figures

Figure A1. Field outcrops of the Purang ophiolitic massif. **(a-b)** Occurrence of meter-scale gabbro and dolerite intrusives in the Puang peridotites. **(c)** Occurrence of ultra-refractory harzburgite (spinel Cr# >0.6) within less refractory harzburgite. **(d)** Occurrence of centimeter-scale orthopyroxenite veins within the harzburgite unit. **(e)** Occurrence of centimeter-scale dunite veins within the lherzolite unit. **(f)** Dunite lenses collected from the harzburgite unit.

Figure A2. (a) SiO_2–FeO*(FeO^{total})/MgO plot (Miyashiro,1974), **(b)** MgO–TiO_2 plot, **(c)** Zr/Yr–Zr plot (Pearce, 1982), and **(d)** V–Ti systematics (Shervais, 1982; Pearce, 2014) for MORB-like mafic rocks data reported from the western and central segment of the suture. Data reported from western segment of the suture include the Purang and Dongbo ophiolites from the southern belt (Miller et al., 2003; Liu et al., 2011, 2013, 2018b; Cheng et al., 2018; Zheng et al., 2019; Xiong et al., 2020), and the Baer and Cuobuzha ophiolites from the northern belt (Liu et al., 2015a, b; Zheng et al., 2017; Liu et al., 2018a). Data reported from the central segment of the suture include the Xigaze ophiolites (Dubois-Cote et al., 2005; Li et al., 2013; Bao et al., 2013; Dai et al., 2013; Zhang et al., 2016; Yang et al., 2017). Data sources for MORB-like Geotimes lava from the Oman ophiolite (Macleod et al., 2013 and reference therein), global mid-ocean ridge basalts (MORB, Gale et al., 2013), boninite from Chichijima Island (Taylor et al., 1994), tholeiitic and calcalkaline lavas from Hahajima Island (Taylor and Nesbitt, 1995) and Izu-Bonin-Mariana forearc basalt (Reagan et al., 2010, 2013; Ishizuka et al., 2011; Shervais et al., 2019). Brown dotted lines in **(b)** show liquid line of descent of basaltic magma modeled with various initial water contents (cf. Macleod et al. 2013).

Figure A3. TiO_2 versus Na_2O contents in spinel-hosted amphibole inclusions (grey triangles) in the low-Cr# dunites. Inset is backscattered electron image showing amphibole inclusions in spinels. Spinel-hosted amphibole inclusions in rocks from modern mid-ocean ridge (MAR: Mid-Atlantic oceanic ridge; CIR: Central Indian oceanic ridge; EPR: Eastern Pacific oceanic ridge) and forearc systems (Morishita et al. 2011, Tamura et al., 2016) are shown for comparison.

Figure A4. Lithium concentrations and isotopic compositions in coexisting silicate minerals from representative Purang peridotites. Grey fields are the ranges of 'normal' mantle values (e.g., Seitz and Woodland 2000; Seitz et al., 2004).

Figure A5. Detailed cross section of a dunite-lherzolite traverse (oxides= wt%). Dunite is plotted as sand-yellow diamonds, transitions (harzburgite) and lherzolite as light-green and dark-green diamonds, respectively.

Supplemental Tables

Table A1. Modal abundances of selected Purang peridotites.

Table A2. Whole-rock major-element compositions of the Purang peridotites.

Table A3. Whole-rock Re-Os isotopic compositions of the Purang peridotites.

Table A4. Major-element compositions of minerals in the Purang peridotites.

Table A5. Trace-element compositions of clinopyroxenes in the Purang peridotites.

Table A6. Averaged lithium isotopes of minerals in the Purang peridotites.

Table A7. Li elemental and isotopic compositions of minerals in the Purang peridotites.

Supplemental Figures

Figure A1. Field outcrops of the Purang ophiolitic massif. **(a-b)** Occurrence of meter-scale gabbro and dolerite intrusives in the Puang peridotites. **(c)** Occurrence of ultra-refractory harzburgite (spinel Cr# >0.6) within less refractory harzburgite. **(d)** Occurrence of centimeter-scale orthopyroxenite veins within the harzburgite unit. **(e)** Occurrence of centimeter-scale dunite veins within the lherzolite unit. **(f)** Dunite lenses collected from the harzburgite unit.

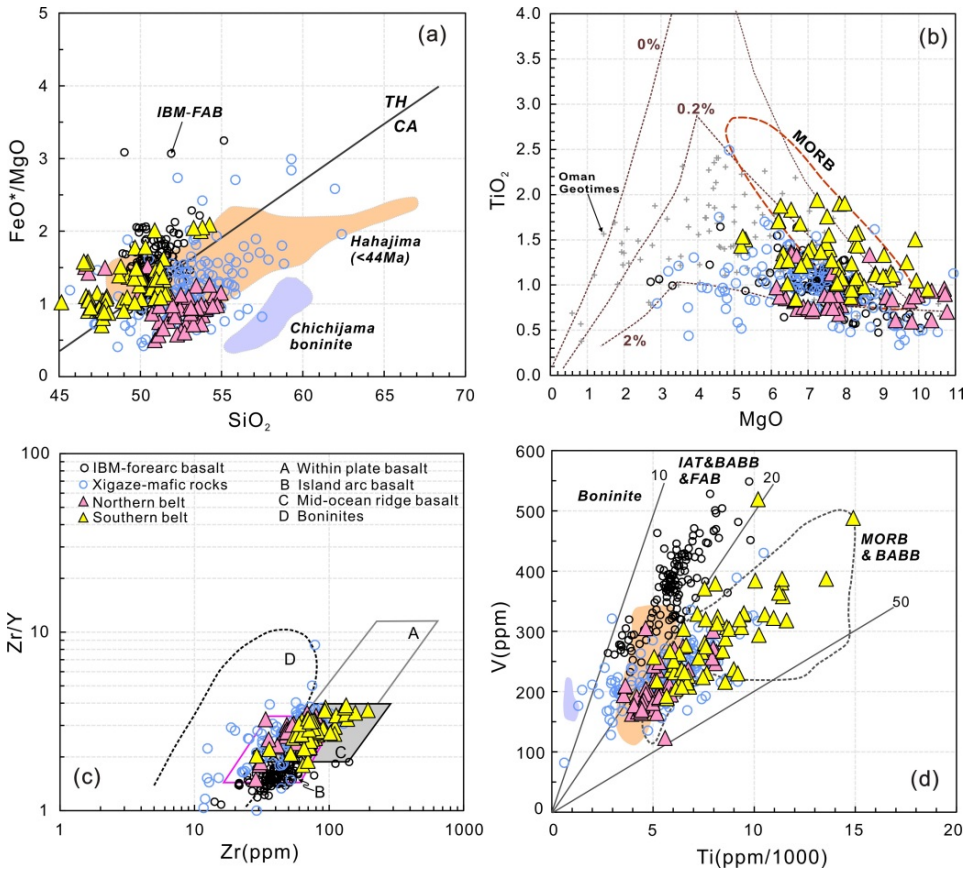

Figure A2. (a) SiO_2–FeO*(FeO^{total})/MgO plot (Miyashiro,1974), **(b)** MgO–TiO_2 plot, **(c)** Zr/Yr–Zr plot (Pearce, 1982), and **(d)** V–Ti systematics (Shervais, 1982; Pearce, 2014) for MORB-like mafic rocks data reported from the western and central segment of the suture. Data reported from western segment of the suture include the Purang and Dongbo ophiolites from the southern belt (Miller et al., 2003; Liu et al., 2011, 2013, 2018b; Cheng et al., 2018; Zheng et al., 2019; Xiong et al., 2020), and the Baer and Cuobuzha ophiolites from the northern belt (Liu et al., 2015a, b; Zheng et al., 2017; Liu et al., 2018a). Data reported from the central segment of the suture include the Xigaze ophiolites (Dubois-Cote et al., 2005; Li et al., 2013; Bao et al., 2013; Dai et al., 2013; Zhang et al., 2016; Yang et al., 2017). Data sources for MORB-like Geotimes lava from the Oman ophiolite (Macleod et al., 2013 and reference therein), global mid-ocean ridge basalts (MORB, Gale et al., 2013), boninite from Chichijima Island (Taylor et al., 1994), tholeiitic and calcalkaline lavas from Hahajima Island (Taylor and Nesbitt, 1995) and Izu-Bonin-Mariana forearc basalt (Reagan et al., 2010, 2013; Ishizuka et al., 2011; Shervais et al., 2019). Brown dotted lines in **(b)** show liquid line of descent of basaltic magma modeled with various initial water contents (cf. Macleod et al. 2013).

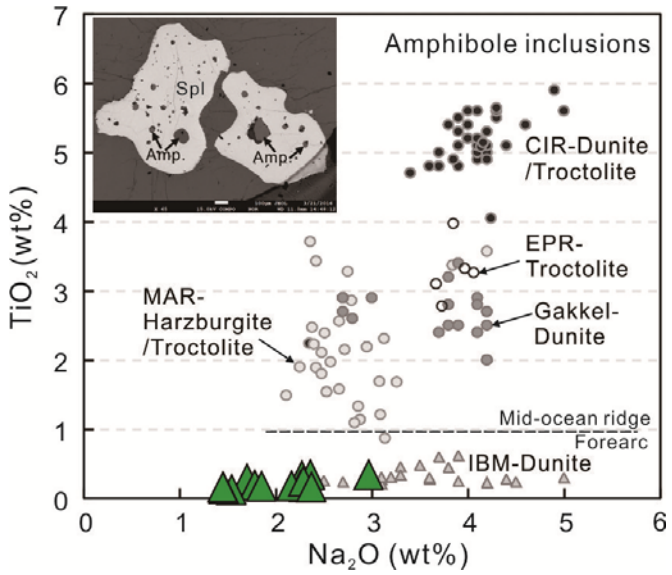

Figure A3. TiO_2 versus Na_2O contents in spinel-hosted amphibole inclusions (grey triangles) in the low-Cr# dunites. Inset is backscattered electron image showing amphibole inclusions in spinels. Spinel-hosted amphibole inclusions in rocks from modern mid-ocean ridge (MAR: Mid-Atlantic oceanic ridge; CIR: Central Indian oceanic ridge; EPR: Eastern Pacific oceanic ridge) and forearc systems (Morishita et al. 2011, Tamura et al., 2016) are shown for comparison.

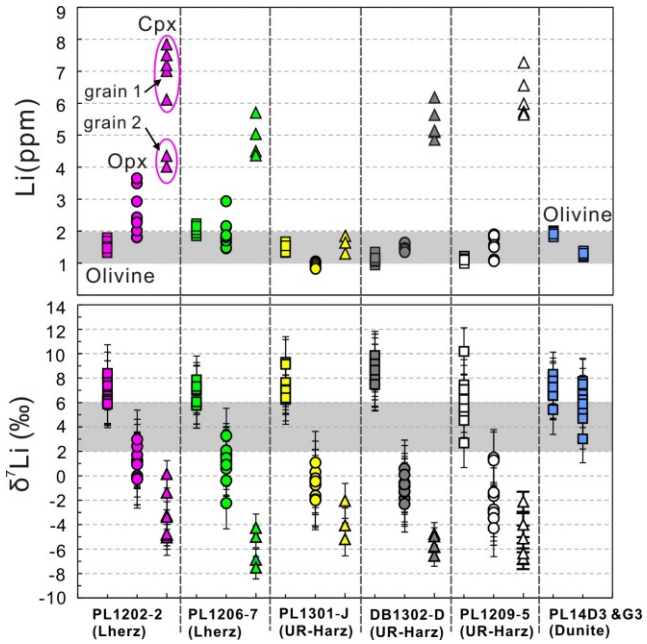

Figure A4. Lithium concentrations and isotopic compositions in coexisting silicate minerals from representative Purang peridotites. Grey fields are the ranges of 'normal' mantle values (e.g., Seitz and Woodland 2000; Seitz et al., 2004).

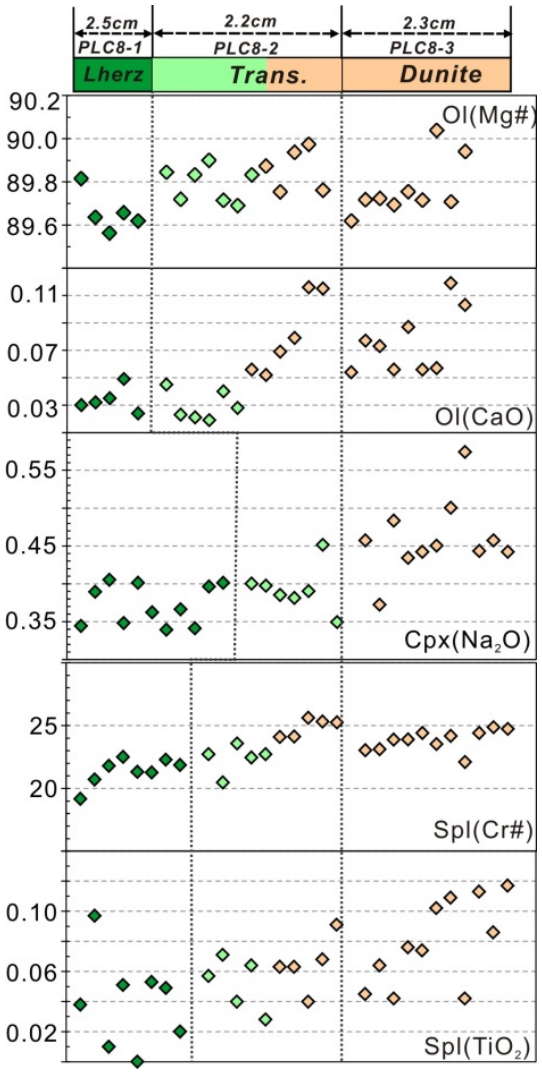

Figure A5. Detailed cross section of a dunite-lherzolite traverse (oxides= wt%). Dunite is plotted as sand-yellow diamonds, transitions (harzburgite) and lherzolite as light-green and dark-green diamonds, respectively.

Supplemental Tables

Table A1 Modal abundances of selected Purang peridotites.

Sample	GPS		Rock Type	Serpentinisation degree	Olivine	Opx	Cpx	Spinel	Total
PL1202-2[#]	30°39'35.02"N	81° 7'3.23"E	Lherz	80%	57	33	9	1	100
PL1202-3[#]	30°39'35.02"N	81° 7'3.23"E	Lherz	80%	60	32	7	1	100
PL1206-7[#]	30°38'57.85"N	81° 7'15.68"E	Lherz	20%	60	32	8	1	100
PL1301-J	30°45'57.40"N	80°51'1.16"E	Harz	5%	66	31	3	1	100
DB1302-D	31°00'13.43"N	80° 19'33.68"E	Harz	5%	68	28	3	1	100
DB1303-I	31°00'02.57"N	80° 19'06.80"E	Harz	5%	78	21	1	1	100
PL1209-5[#]	30°35'24.04"N	81° 9'3.15"E	Harz	50%	73	26	1	1	100
PL1419-1	30°39'0.95"N	81° 2'28.33"E	Harz	10%	72	27	1	1	100
DB1303-II	31°00’02.57"N	80° 19'06.80"E	Harz	5%	70	29	1	1	100
PL14D3	30°37'9.76"N	81° 8'28.15"E	Dunite	60%	99	-	1	1	100
PL14F1	30°36'38.30"N	81° 9'11.25"E	Dunite	50%	100	-	-	1	100
PL14G4	30°36'26.39"N	81° 9'55.37"E	Dunite	20%	97	-	2	1	100
PL1405-3	30°33'9.39"N	81°14'36.12"E	Dunite	80%	98	-	1	1	100
PL14C8-1	30°38'6.24"N	81° 7'41.30"E	Lherz	50%	59	33	8	1	100
PL14C8-2	30°38'6.24"N	81° 7'41.30"E	Harz	50%	75	23	2	1	100
PL14C8-3	30°38'6.24"N	81° 7'41.30"E	Dunite	60%	98	-	1	1	100

#: sample reported in previous studies (Gong et al. 2016, 2020); Opx: orthopyroxene; Cpx: clinopyroxene; Lherz: lherzolite; Harz: harzburgite.
Modal abundances were calculated by the least-squares method from whole-rock and mineral major-element compositions.
No orthopyroxene was observed in the dunites.
Degree of serpentinisation was estimated by thin section observation and loss on ignition.

Table A2 Whole-rock major-element compositions of the Purang peridotites.

Sample	SiO_2	TiO_2	Al_2O_3	$^{T}Fe_2O_3$	MnO	MgO	CaO	K_2O	P_2O_5	LOI	Total	Mg#	FeO*
Lherzolite													
PL1202-2[#]	41.46	0.04	2.27	8.01	0.12	35.79	2.34	0.02	<0.01	10.03	100.09	89.9	7.21
PL1202-3[#]	40.24	0.03	2.13	8.02	0.12	36.40	2.27	0.02	<0.01	10.83	100.07	90.0	7.22
PL1206-7[#]	44.04	0.03	2.21	8.58	0.13	39.48	2.21	0.01	<0.01	2.80	99.51	90.1	7.72
Harzburgite													
PL1301-J	44.62	<0.01	1.02	8.71	0.13	43.55	1.20	<0.01	<0.01	-0.22	99.03	90.8	7.84
DB1302D	44.55	<0.01	1.04	8.64	0.12	44.31	1.05	<0.01	<0.01	-0.12	99.61	91.0	7.77
DB1302D-dup	44.13	0.01	1.04	8.60	0.12	44.13	1.04	<0.01	<0.01	-0.12	98.96	91.0	7.74
DB1303-I	43.25	<0.01	0.60	9.46	0.13	45.64	0.64	<0.01	<0.01	-0.36	99.38	90.5	8.51
PL1209-5[#]	41.90	<0.01	0.43	8.53	0.12	41.50	0.62	0.02	<0.01	6.91	100.04	90.6	7.68
PL1419-1	43.82	<0.01	0.33	8.66	0.13	44.75	0.49	<0.01	<0.01	1.32	99.52	91.1	7.79
DB1303-II	44.52	<0.01	0.63	8.49	0.12	45.42	0.72	<0.01	<0.01	-0.18	99.74	91.4	7.64
Dunite													
PL14D3	37.04	<0.01	0.07	9.29	0.12	44.73	0.16	<0.01	<0.01	8.76	100.18	90.5	8.36
PL14F1	38.08	<0.01	0.16	9.67	0.13	45.88	0.30	<0.01	<0.01	6.47	100.71	90.4	8.70
PL14G4	40.37	<0.01	0.17	8.82	0.12	48.16	0.23	<0.01	<0.01	1.64	99.53	91.5	7.94
PL1405-3	36.42	<0.01	0.15	7.34	0.10	45.31	0.16	<0.01	<0.01	10.55	100.05	92.4	6.60
Lherzolite-transition-dunite traverse													
PL14C8-1	42.26	0.04	2.02	8.48	0.12	37.70	2.34	0.01	0.01	7.05	100.03	89.8	7.63
PL14C8-2	39.97	0.02	1.15	9.17	0.12	40.94	1.17	0.01	0.01	7.24	99.80	89.8	8.25
PL14C8-3	37.10	<0.01	0.21	9.95	0.12	44.15	0.28	0.01	0.01	9.13	100.96	89.8	8.95

#: data reported in previous studies (Gong et al., 2016, 2020)

LOI: loss on ignition; $FeO^{T} = {}^{T}Fe_2O_3 \times 0.8998$; oxides= wt%; dup: duplicate analysis.

Na_2O contents below detection limit.

Table A3 Whole-rock Re-Os isotopic compositions of the Purang peridotites.

Sample	Re(ppb)	2SE	Os(ppb)	2SE	$^{187}Re/^{188}Os$	2SE	$^{187}Os/^{188}Os$	2SE	T_{RD}	Al_2O_3(wr)	Spinel Cr#
Lherzolite											
PL1202-2#	0.34	0.004	4.87	0.005	0.3388	0.0041	0.1276	0.0002	0.4	2.27	0.18
PL1202-3#	0.27	0.004	4.41	0.004	0.2921	0.0048	0.1262	0.0001	0.6	2.13	0.18
PL1206-7#	0.30	0.004	4.49	0.003	0.3168	0.0040	0.1266	0.0002	0.6	2.21	0.16
Harzburgite											
PL1301-J	0.32	0.004	5.14	0.004	0.2958	0.0039	0.1269	0.0002	0.5	1.02	0.42
DB1302-D	0.14	0.002	3.38	0.002	0.2020	0.0030	0.1271	0.0002	0.4	1.04	0.40
DB1303-I	0.31	0.002	5.16	0.005	0.2876	0.0023	0.1266	0.0002	0.5	0.60	0.56
PL1209-5	0.45	0.005	5.14	0.005	0.4180	0.0049	0.1260	0.0002	0.7	0.43	0.64
PL1419-1	0.03	0.001	3.77	0.003	0.0368	0.0010	0.1253	0.0002	0.6	0.33	0.72
DB1303-II	0.01	0.001	4.10	0.003	0.0155	0.0009	0.1264	0.0002	0.5	0.63	0.56
Dunite											
PL14D3	0.01	0.001	0.44	0.000	0.1018	0.0063	0.1302	0.0003		0.07	0.55
PL14F1	0.00	0.001	1.02	0.001	0.0230	0.0059	0.1302	0.0003		0.16	0.36
PL14G4	0.01	0.001	4.36	0.003	0.0104	0.0007	0.1240	0.0002	0.9	0.17	0.68
PL14G4-dup	0.01	0.001	5.54	0.005	0.0114	0.0008	0.1239	0.0002	0.9		0.68
PL1405-3	0.12	0.002	5.73	0.005	0.1006	0.0018	0.1272	0.0002		0.15	0.75
Lherzolite-transition-dunite traverse											
PL14C8-1	0.35	0.003	4.42	0.003	0.3852	0.0028	0.1290	0.0001	0.2	2.02	0.21
PL14C8-2	0.17	0.003	3.07	0.002	0.2675	0.0050	0.1296	0.0002	0.1	1.15	0.24
PL14C8-3	0.01	0.001	2.56	0.002	0.0224	0.0019	0.1341	0.0002		0.21	0.24
WPR-1	10.85	0.19	16.31	0.03	3.21	0.06	0.1445	0.0001		-	-
WPR-1	10.72	0.1	16.16	0.05	3.2	0.03	0.1445	0.0003		-	-
Chu et al. (2015)	10.78	0.19	16.78	0.58	3.23	0.05	0.1447	0.0001		-	-
Li et al. (2015)	10.98	0.12	15.71	0.22	3.3	0.1	0.1445	0.0002		-	-
Huang et al. (2018)	10.86	0.08	16.16	0.19	3.24	0.05	0.1446	0.0001		-	-

#: data reported in previous study (Gong et al. 2020). dup.: duplicate analysis; wr: whole-rock

The uncertainty (standard error: SE) in the analyzed data was obtained through error propagation from isotope dilution.

Two reference material (WPR-1) analyzed here are within error similar to those reported in literatures.

T_{RD} model ages are calculated based on the primitive upper mantle (PUM; $^{187}Re/^{188}Os = 0.402$; $^{187}Os/^{188}Os = 0.1296$, Meisel et al., 2001).

Table A4-1. Major-element compositions of olivines in the Purang peridotites.

Sample	N.	SiO_2	TiO_2	Al_2O_3	Cr_2O_3	FeO*	MnO	MgO	NiO	CaO	Na_2O	K_2O	Total	Mg#
Lherzolite														
PL1202-2[#]	6	40.75	0.02	<0.01	0.01	9.74	0.15	48.55	0.39	0.03	<0.01	<0.01	99.7	89.9
	1σ	0.30	0.03	<0.01	0.02	0.24	0.04	0.31	0.03	<0.01	<0.01	<0.01		
PL1202-3[#]	8	40.77	<0.01	0.01	0.01	9.71	0.14	49.54	0.37	0.03	<0.01	<0.01	100.6	90.1
	1σ	0.19	0.01	0.01	0.02	0.10	0.03	0.39	0.03	0.01	<0.01	<0.01		
PL1206-7[#]	5	40.84	<0.01	0.01	0.01	9.58	0.13	49.89	0.37	0.02	<0.01	<0.01	100.9	90.3
	1σ	0.41	0.01	0.01	0.01	0.11	0.01	0.36	0.05	0.02	<0.01	<0.01		
Harzburgite														
PL1301-J	9	40.32	<0.01	<0.01	<0.01	9.36	0.13	50.11	0.41	0.03	<0.01	<0.01	100.4	90.5
	1σ	0.21	<0.01	<0.01	<0.01	0.15	0.02	0.19	0.03	0.02	<0.01	<0.01		
DB1302-D	8	40.48	<0.01	<0.01	<0.01	8.90	0.13	50.28	0.41	0.02	<0.01	<0.01	100.3	91.0
	1σ	0.13	0.01	0.01	<0.01	0.13	0.02	0.14	0.04	0.01	<0.01	<0.01		
DB1303-I	9	40.34	<0.01	<0.01	<0.01	9.30	0.13	49.56	0.37	0.03	<0.01	<0.01	99.7	90.5
	1σ	0.27	<0.01	<0.01	0.01	0.27	0.03	0.21	0.02	0.01	<0.01	<0.01		
PL1209-5[#]	10	41.36	0.02	0.02	0.02	8.70	0.11	49.29	0.36	0.03	0.02	<0.01	99.9	91.0
	1σ	0.32	0.01	0.01	<0.01	0.23	0.03	0.37	0.07	<0.01	<0.01	<0.01		
PL1419-1	3	40.94	-	-	0.02	8.39	0.13	50.53	0.40	0.02	0.01	<0.01	100.4	91.5
	1σ	0.06	-	-	0.02	0.33	0.01	0.19	0.03	0.02	0.01	<0.01		
DB1303-II	10	40.15	<0.01	<0.01	<0.01	8.73	0.13	50.22	0.38	0.02	<0.01	<0.01	99.7	91.1
	1σ	0.12	0.01	<0.01	<0.01	0.20	0.02	0.18	0.02	<0.01	<0.01	<0.01		
Dunite														
PL14D3	6	40.79	<0.01	<0.01	0.01	9.19	0.13	50.13	0.39	0.07	0.03	<0.01	100.8	90.7
	1σ	0.17	0.01	<0.01	0.01	0.19	0.02	0.27	0.03	0.03	0.06	<0.01		
PL14F1	7	40.90	<0.01	0.08	0.08	9.31	0.14	49.69	0.33	0.14	<0.01	<0.01	100.7	90.5
	1σ	0.19	<0.01	0.21	0.20	0.23	0.02	0.15	0.03	0.02	<0.01	<0.01		
PL14G4	6	40.96	<0.01	<0.01	<0.01	8.14	0.11	50.79	0.38	0.08	<0.01	<0.01	100.5	91.8
	1σ	0.16	0.01	<0.01	<0.01	0.18	0.02	0.19	0.03	0.01	<0.01	<0.01		
PL1405-3	6	41.11	<0.01	<0.01	<0.01	7.35	0.11	51.82	0.39	0.07	<0.01	<0.01	100.9	92.6
	1σ	0.44	0.02	<0.01	0.01	0.08	0.02	0.40	0.02	0.02	<0.01	<0.01		
Traverse														
PL14C8-1	5	40.48	<0.01	<0.01	0.01	10.10	0.13	49.12	0.39	0.03	0.02	<0.01	100.3	89.7
	1σ	0.23	<0.01	<0.01	0.01	0.10	0.02	0.43	0.03	<0.01	0.02	<0.01		
PL14C8-2	12	40.79	<0.01	<0.01	<0.01	10.00	0.13	49.50	0.37	0.06	0.01	<0.01	100.9	89.8
	1σ	0.16	<0.01	<0.01	0.01	0.09	0.02	0.25	0.01	0.03	<0.01	<0.01		
PL14C8-3	9	40.86	<0.01	<0.01	<0.01	10.09	0.13	49.63	0.36	0.08	<0.01	<0.01	101.2	89.8
	1σ	0.21	<0.01	<0.01	0.01	0.15	0.02	0.19	0.02	0.02	<0.01	<0.01		

#: sample reported in previous studies (Gong et al. 2016, 2020).

Mg#= 100* $Mg^{2+}/(Mg^{2+}+ Fe_{tot}^{2+})$; N: number of analysis; σ: standard deviation of the mean.

Table A4-2 Major-element compositions of orthopyroxenes in the Purang peridotites.

Sample	N.	SiO_2	TiO_2	Al_2O_3	Cr_2O_3	FeO*	MnO	MgO	NiO	CaO	Na_2O	K_2O	Total	Mg#	Cr#
Lherzolite															
PL1202-2#	10	54.37	0.06	5.00	0.76	6.11	0.14	31.36	0.10	1.82	0.04	<0.01	99.75	90.1	9.2
	1σ	0.64	0.03	0.37	0.07	0.27	0.03	0.86	0.02	1.00	0.02	<0.01			
PL1202-3#	4	54.33	0.08	5.12	0.74	6.11	0.14	31.79	0.10	1.78	0.05	<0.01	100.24	90.3	8.8
	1σ	0.25	0.03	0.15	0.07	0.10	0.03	0.33	0.02	0.59	0.02	0.01			
PL1206-7#	4	54.42	0.07	5.00	0.73	6.10	0.12	32.37	0.08	1.32	0.03	<0.01	100.24	90.4	8.9
	1σ	0.46	0.02	0.61	0.20	0.14	0.01	0.53	0.02	0.41	0.01	0.01			
Harzburgite															
PL1301-J	11	55.09	0.02	2.75	0.74	5.99	0.13	33.96	0.10	0.76	0.00	<0.01	99.56	91.0	15.4
	1σ	0.31	0.02	0.27	0.13	0.11	0.02	0.29	0.02	0.15	0.01	<0.01			
DB1302-D	7	55.04	0.03	3.04	0.73	5.80	0.12	33.86	0.09	0.84	0.00	<0.01	99.55	91.2	13.9
	1σ	0.37	0.03	0.21	0.08	0.08	0.02	0.24	0.01	0.21	0.01	<0.01			
DB1303-I	8	55.18	0.01	2.61	0.73	5.99	0.15	33.73	0.11	0.74	0.00	<0.01	99.26	90.9	15.8
	1σ	0.34	0.01	0.31	0.06	0.18	0.01	0.23	0.02	0.23	0.00	<0.01			
PL1209-5#	7	57.48	0.02	1.34	0.53	5.54	0.15	33.35	0.11	1.34	0.02	<0.01	99.89	91.5	21.0
	1σ	0.50	0.01	0.05	0.09	0.10	0.03	0.59	0.04	0.80	0.01	<0.01			
PL1419-1	3	57.34	0.01	0.94	0.37	5.62	0.13	34.96	0.11	0.73	0.00	0.02	100.22	91.7	20.9
	1σ	0.08	0.01	0.02	0.01	0.08	0.03	0.13	0.01	0.15	0.00	0.01			
DB1303-II	7	55.33	0.02	1.93	0.69	5.57	0.14	34.14	0.10	1.09	0.01	<0.01	99.03	91.6	19.5
	1σ	0.19	0.01	0.05	0.02	0.09	0.03	0.28	0.03	0.16	0.00	<0.01			
Traverse															
PL14C8-1	7	54.31	0.05	4.67	0.77	6.40	0.13	32.05	0.08	1.75	0.02	<0.01	100.25	89.9	10.0
	1σ	0.30	0.02	0.29	0.08	0.23	0.02	0.45	0.01	0.56	0.02	0.01			
PL14C8-2	8	54.65	0.08	4.46	0.75	6.42	0.14	32.34	0.07	1.61	0.03	0.01	100.57	90.0	10.1
	1σ	0.37	0.02	0.32	0.07	0.06	0.02	0.37	0.03	0.29	0.01	0.01			

#: sample reported in previous studies (Gong et al. 2016, 2020).

Mg#= 100* $Mg^{2+}/(Mg^{2+}+Fe_{tot}^{2+})$; Cr#= 100*$Cr^{3+}/(Cr^{3+}+Al^{3+})$; N: number of analysis; σ: standard deviation of the mean

Table A4-3 Major-element compositions of clinopyroxenes in the Purang peridotites.

Sample	N.	SiO_2	TiO_2	Al_2O_3	Cr_2O_3	FeO*	MnO	MgO	NiO	CaO	Na_2O	K_2O	Total	Mg#	Cr#
Lherzolite															
PL1202-2#	6	51.29	0.19	5.99	1.13	2.76	0.09	15.98	0.06	21.82	0.48	<0.01	99.79	91.2	11.2
	1σ	0.45	0.02	0.26	0.08	0.33	0.03	0.93	0.05	1.22	0.06	<0.01			
PL1202-3#	3	51.05	0.18	6.32	1.17	2.63	0.11	15.88	0.04	21.51	0.48	<0.01	99.37	91.5	11.1
	1σ	0.18	0.01	0.13	0.06	0.06	0.03	0.41	0.03	0.53	0.03	<0.01			
PL1206-7#	2	51.23	0.18	6.26	1.24	2.69	0.14	15.93	0.04	21.26	0.57	<0.01	99.54	91.3	11.8
	1σ	0.01	0.05	0.00	0.02	0.15	0.00	0.36	0.00	0.47	0.04	<0.01			
Harzburgite															
PL1301-J	14	52.08	0.06	3.06	1.02	2.16	0.08	17.41	0.05	22.93	0.03	<0.01	98.89	93.5	18.3
	1σ	0.39	0.02	0.27	0.16	0.15	0.02	0.33	0.03	0.37	0.02	<0.01			
DB1302-D	9	51.65	0.07	3.49	1.18	2.05	0.08	16.81	0.05	23.09	0.06	<0.01	98.53	93.6	18.5
	1σ	0.30	0.03	0.38	0.12	0.18	0.02	0.25	0.03	0.32	0.01	<0.01			
DB1303-I	4	52.02	0.04	3.12	0.93	2.13	0.07	17.01	0.04	22.97	0.07	<0.01	98.40	93.4	16.7
	1σ	0.42	0.01	0.46	0.17	0.09	0.04	0.41	0.03	0.10	0.01	<0.01			
PL1209-5#	5	54.39	0.04	1.59	0.86	1.98	0.07	17.31	0.06	23.60	0.16	<0.01	100.06	94.0	26.6
	1σ	0.24	0.01	0.11	0.02	0.12	0.03	0.17	0.04	0.27	0.01	<0.01			
PL1419-1	4	54.52	0.03	0.97	0.61	1.75	0.06	18.12	0.05	23.53	0.11	<0.01	99.74	94.9	29.6
	1σ	0.33	0.02	0.08	0.04	0.07	0.01	0.08	0.02	0.23	0.02	<0.01			
DB1303-II	7	52.82	0.04	2.09	0.96	1.94	0.08	17.58	0.05	23.11	0.12	<0.01	98.79	94.2	23.5
	1σ	0.26	0.03	0.18	0.16	0.16	0.03	0.26	0.02	0.37	0.02	<0.01			
Dunite															
PL14D3	2	53.36	0.03	2.18	0.89	2.22	0.07	17.35	0.04	23.07	0.23	<0.01	99.43	93.3	21.5
	1σ	0.22	0.05	0.19	0.03	0.03	0.02	0.36	0.03	0.35	0.04	<0.01			
PL14G4	3	54.27	0.04	1.41	0.87	1.34	0.05	17.26	0.01	24.27	0.31	<0.01	99.83	95.8	29.1
	1σ	0.12	0.03	0.12	0.12	0.12	0.01	0.14	0.01	0.18	0.04	<0.01			
PL1405-3	4	53.90	0.04	0.75	0.41	1.32	0.02	17.84	0.04	24.50	0.08	<0.01	98.91	96.0	26.9
	1σ	0.75	0.03	0.17	0.10	0.17	0.01	0.21	0.03	0.49	0.02	<0.01			
Traverse															
PL14C8-1	6	51.41	0.14	5.64	1.18	2.76	0.10	15.82	0.03	22.23	0.37	<0.01	99.68	91.1	12.3
	1σ	0.29	0.03	0.12	0.08	0.16	0.02	0.21	0.02	0.34	0.03	<0.01			
PL14C8-2	7	51.38	0.17	5.41	1.12	2.74	0.10	16.37	0.06	21.76	0.39	<0.01	99.49	91.4	12.2
	1σ	0.34	0.01	0.28	0.05	0.30	0.02	0.96	0.01	1.20	0.03	<0.01			
PL14C8-3	11	51.49	0.17	5.29	1.12	2.70	0.08	16.17	0.05	22.36	0.46	<0.01	99.90	91.4	12.5
	1σ	0.29	0.04	0.29	0.09	0.21	0.02	0.53	0.03	0.71	0.05	<0.01			

#: sample reported in previous studies (Gong et al. 2016, 2020).

Mg#= 100* $Mg^{2+}/(Mg^{2+}+Fe_{tot}^{2+})$; Cr#= 100*$Cr^{3+}/(Cr^{3+}+Al^{3+})$; N: number of analysis; σ: standard deviation of the mean

Table A4-4 Major-element compositions of spinels in the Purang peridotites.

Sample	N.	SiO_2	TiO_2	Al_2O_3	Cr_2O_3	FeO	MnO	MgO	NiO	CaO	Na_2O	K_2O	Total	Mg#	Cr#
Lherzolite															
PL1202-2[#]	6	0.23	0.06	49.96	16.60	12.60	0.14	17.94	0.31	<0.01	0.01	<0.01	97.85	71.7	18.2
	1σ	0.03	0.02	0.97	1.25	0.18	0.02	0.20	0.02	0.01	<0.01	<0.01			
PL1202-3[#]	2	0.10	0.04	49.13	16.54	13.75	0.13	17.93	0.31	0.02	<0.01	<0.01	97.96	69.9	18.4
	1σ	0.13	0.02	0.27	0.04	0.05	0.03	0.13	0.00	<0.01	<0.01	<0.01			
PL1206-7[#]	2	0.19	0.05	51.47	14.81	12.53	0.09	18.47	0.30	0.04	<0.01	<0.01	97.99	72.4	16.2
	1σ	0.11	<0.01	2.69	2.77	0.95	0.02	0.81	0.01	0.01	<0.01	<0.01			
Harzburgite															
PL1301-J	4	0.05	0.02	32.68	35.32	15.87	0.17	14.59	0.12	<0.01	<0.01	<0.01	98.82	62.1	42.0
	1σ	0.02	0.02	0.56	0.43	0.48	0.01	0.22	0.03	<0.01	<0.01	<0.01			
DB1302-D	8	0.02	0.04	33.69	34.02	15.87	0.14	14.69	0.15	0.01	<0.01	<0.01	98.65	62.3	40.4
	1σ	0.02	0.02	1.06	1.05	0.49	0.03	0.21	0.03	0.01	0.01	<0.01			
DB1303-I	9	0.03	0.05	22.83	43.98	19.96	0.22	11.39	0.07	<0.01	<0.01	<0.01	98.54	50.4	56.4
	1σ	0.03	0.02	1.38	1.49	0.51	0.03	0.17	0.04	<0.01	0.01	<0.01			
PL1209-5[#]	7	0.09	0.07	18.60	49.79	20.34	0.30	10.86	0.10	<0.01	0.02	<0.01	100.17	48.8	64.2
	1σ	0.07	0.02	0.70	1.11	0.78	0.05	0.46	0.03	<0.01	0.01	<0.01			
PL1419-1	5	0.01	0.11	13.77	51.86	22.82	0.28	9.15	0.06	0.01	0.04	<0.01	98.12	41.7	71.6
	1σ	0.02	0.02	0.64	0.63	0.64	0.03	0.06	0.02	0.01	0.03	<0.01			
DB1303-II	7	0.04	0.06	23.72	44.95	17.36	0.19	12.47	0.08	<0.01	<0.01	<0.01	98.89	56.2	56.0
	1σ	0.01	0.02	0.48	0.54	0.31	0.01	0.24	0.02	<0.01	<0.01	<0.01			
Dunite															
PL14D3	5	0.04	0.08	22.17	39.67	24.53	0.23	11.38	0.14	0.01	<0.01	<0.01	98.25	45.3	54.5
	1σ	0.03	0.01	2.12	2.33	1.34	0.02	0.94	0.03	0.01	0.01	<0.01			
PL14F1	5	0.13	0.12	33.28	28.03	21.49	0.18	13.86	0.20	0.02	<0.01	<0.01	97.31	53.5	36.1
	1σ	0.11	0.02	2.91	3.38	1.53	0.01	0.67	0.06	0.01	<0.01	<0.01			
PL14G4	6	0.02	0.10	16.46	51.52	18.16	0.20	11.97	0.07	0.02	0.01	<0.01	98.53	54.0	67.7
	1σ	0.03	0.01	0.59	0.80	0.27	0.03	0.18	0.02	0.02	0.02	<0.01			
PL1405-3	7	0.01	0.10	12.40	54.55	21.24	0.26	10.05	0.05	<0.01	0.01	<0.01	98.69	45.8	74.7
	1σ	0.01	0.02	0.55	0.66	0.52	0.04	0.32	0.02	<0.01	0.01	<0.01			
Traverse															
PL14C8-1	7	0.15	0.05	47.22	19.13	13.55	0.11	17.48	0.28	0.01	0.03	0.01	98.02	69.7	21.4
	1σ	0.07	0.03	0.70	1.02	0.48	0.02	0.21	0.03	0.01	0.02	0.02			
PL14C8-2	8	0.02	0.06	44.87	21.32	14.68	0.11	16.95	0.24	<0.01	0.01	<0.01	98.28	67.3	24.2
	1σ	0.03	0.02	0.98	0.89	0.52	0.02	0.23	0.02	<0.01	0.01	<0.01			
PL14C8-3	9	0.08	0.08	44.51	20.85	15.49	0.14	17.06	0.26	0.03	0.01	<0.01	98.52	66.3	23.9
	1σ	0.17	0.03	0.58	0.83	0.44	0.02	0.22	0.04	0.07	<0.01	<0.01			

#: sample reported in previous studies (Gong et al. 2016, 2020).

Mg#= 100* $Mg^{2+}/(Mg^{2+}+Fe_{tot}^{2+})$; Cr#= 100*$Cr^{3+}/(Cr^{3+}+Al^{3+})$; N: number of analysis; σ: standard deviation of the mean

Table A4-5 Major-element compositions of spinel-hosted amphiboles in the Purang peridotites.

Sample	PL14D3					DB1303-I				
Rock type	Dunite					Harzburgite				
Point	Amp-1	Amp-2	Amp-3	Amp-4	Amp-5	Amp-1	Amp-2	Amp-3	Amp-4	Amp-5
SiO_2	47.12	46.44	47.75	46.39	47.01	48.23	49.23	48.35	47.58	48.17
TiO_2	0.18	0.17	0.18	0.24	0.16	0.19	0.11	0.17	0.15	0.15
Al_2O_3	9.37	9.57	8.98	9.58	9.14	8.31	8.12	7.67	8.85	9.10
Cr_2O_3	2.79	2.96	2.93	2.81	2.91	3.27	2.15	3.23	3.22	3.33
FeO	3.71	3.71	3.45	3.87	3.74	3.08	2.69	3.17	3.25	3.12
MnO	0.03	0.07	0.06	0.03	0.04	0.02	0.03	0.07	0.05	0.05
MgO	19.97	19.94	20.40	19.81	19.96	20.40	20.28	20.51	20.15	20.31
NiO	0.08	0.14	0.11	0.11	0.07	0.10	0.12	0.09	0.09	0.09
CaO	11.88	11.70	11.95	11.69	11.69	11.64	12.29	11.39	11.56	11.71
Na_2O	2.25	2.30	2.16	2.29	2.37	1.42	1.22	1.49	1.58	1.62
K2O	0.30	0.30	0.30	0.32	0.23	0.02	0.01	0.00	0.02	0.02
Cl	-	0.02	0.02	0.03	0.01	-	-	-	-	-
Total	97.7	97.3	98.3	97.2	97.3	96.7	96.2	96.1	96.5	97.7
Mg#	90.6	90.6	91.3	90.1	90.5	92.2	93.1	92.0	91.7	92.1

Amp: amphibole; Mg#= 100* $Mg^{2+}/(Mg^{2+}+Fe_{tot}^{2+})$

Table A5 Trace-element compositions of clinopyroxenes in the Purang peridotites.

Sample	PL1202-2#		PL1202-3#		PL1301-J		DB1302-D		DB1303-I		PL1419-1		PL14D3		PL1405-3		PL14C8-3	
Rock Type	Lherzolite						Harzburgite						Dunite					
N.	8	1σ	2	1σ	2	1σ	4	1σ	2	1σ	2	1σ	3	1σ	2	1σ	3	1σ
ppm																		
Li	-	-	2.6	0.3	2.2	0.3	6.1	1.2	2.8	0.2	2.9	0.4	2.7	2.1	1.4	0.2	12.8	1.7
Sc	56	2	53	3	57	1	55	2	73	9	79	37	67	19	69	5	62	2
Ti	1091	45	1182	95	254	0.4	416	10	236	39	300	159	311	61	172	53	1118	42
V	241	7	231	0.3	219	9	203	9	247	0	178	77	203	27	64	23	284	4
Rb	0.161	0.194	0.120	0.011	0.010	0.014	0.048	0.058	0.001	0.002	0.122	0.172	0.043	0.037	0.240	0.339	0.101	0.089
Sr	0.519	0.045	0.783	0.078	0.058	0.001	0.118	0.108	0.071	0.005	0.550	0.047	2.812	0.222	0.251	0.087	0.322	0.102
Y	9.998	0.297	12.647	1.733	2.481	0.113	4.121	0.113	2.428	0.186	2.372	0.513	3.549	0.334	2.158	0.561	9.922	0.100
Zr	0.455	0.090	0.624	0.047	0.013	0.018	0.023	0.027	<0.001	<0.001	0.090	0.060	1.168	0.299	0.354	0.193	0.315	0.050
Nb	0.011	0.003	0.009	0.003	0.001	0.001	0.003	0.003	0.003	0.002	0.002	0.001	0.004	0.004	0.002	0.003	0.005	0.001
Cs	0.022	0.026	0.006	0.009	0.047	0.066	0.006	0.012	-	-	0.125	0.177	0.010	0.018	0.058	0.081	0.028	0.035
Ba	0.018	0.012	0.555	0.535	0.055	0.063	0.651	0.869	0.005	0.007	0.142	0.102	0.003	0.005	0.298	0.351	0.013	0.013
La	0.002	0.003	0.003	0.005	-	-	<0.001	0.001	-	-	0.017	0.006	0.134	0.020	0.132	0.175	0.003	0.002
Ce	0.012	0.006	0.019	0.009	0.002	<0.001	0.001	<0.001	0.002	<0.001	0.022	0.009	0.238	0.054	0.017	0.018	0.003	0.002
Pr	0.015	0.004	0.023	0.003	-	-	-	-	-	-	0.009	0.001	0.034	0.008	0.003	0.000	0.005	0.003
Nd	0.286	0.062	0.409	0.117	-	-	0.017	0.012	0.008	0.012	0.028	0.028	0.138	0.033	0.026	0.002	0.133	0.011
Sm	0.331	0.037	0.520	0.085	0.015	0.021	0.039	0.008	0.013	0.018	0.048	0.040	0.080	0.028	0.046	0.037	0.185	0.008
Eu	0.179	0.013	0.227	0.019	0.007	0.001	0.018	0.006	0.017	0.001	0.019	0.000	0.030	0.008	0.017	0.001	0.095	0.011
Gd	0.920	0.085	1.450	0.332	0.096	0.013	0.186	0.038	0.116	0.041	0.150	0.021	0.231	0.035	0.137	0.099	0.697	0.056
Tb	0.213	0.019	0.255	0.005	0.028	0.006	0.054	0.006	0.033	0.005	0.043	0.013	0.053	0.005	0.050	0.014	0.178	0.012
Dy	1.696	0.125	1.953	0.010	0.273	0.041	0.516	0.023	0.307	0.004	0.296	0.019	0.535	0.058	0.394	0.083	1.446	0.079
Ho	0.371	0.017	0.484	0.069	0.084	0.003	0.158	0.016	0.087	0.005	0.090	0.021	0.138	0.010	0.079	0.027	0.373	0.023
Er	1.201	0.067	1.422	0.134	0.343	0.049	0.554	0.040	0.307	0.073	0.284	0.020	0.410	0.069	0.212	0.037	1.233	0.030
Tm	0.168	0.021	0.221	0.034	0.058	0.015	0.082	0.014	0.057	0.017	0.048	0.005	0.079	0.008	0.032	0.010	0.187	0.015
Yb	1.222	0.098	1.461	0.184	0.377	0.028	0.540	0.076	0.332	0.043	0.399	0.124	0.500	0.094	0.157	0.083	1.141	0.091
Lu	0.174	0.026	0.205	0.035	0.065	0.006	0.076	0.008	0.052	0.004	0.047	0.026	0.087	0.007	0.021	0.012	0.186	0.008
Hf	0.108	0.018	0.138	0.079	0.016	0.003	0.008	0.008	<0.001	<0.001	-	-	0.044	0.023	0.020	0.028	0.137	0.022
Ta	0.002	0.002	<0.001	<0.001	<0.001	<0.001	<0.001	<0.001	0.009	0.013	-	-	0.001	0.001	0.001	0.001	<0.001	<0.001
Pb	0.012	0.012	0.377	0.531	0.001	0.002	0.008	0.007	0.009	0.003	0.064	0.010	0.063	0.012	1.014	1.180	0.048	0.007
Th	0.001	0.002	<0.001	<0.001	<0.001	<0.001	<0.001	<0.001	<0.001	<0.001	0.002	0.003	0.008	0.001	0.002	0.001	-	-
U	0.002	0.002	<0.001	<0.001	<0.001	<0.001	<0.001	<0.001	-	-	-	-	0.005	0.003	0.001	<0.001	<0.001	0.001

#: sample reported in previous studies (Gong et al. 2020). N: number of analysis. -: below detection limits; σ: standard deviation of the mean

Table A6 Averaged lithium isotopes of minerals in the Purang peridotites.

Sample	Rock type	Mineral	N	δ^7Li(‰)	2SE	Li(ppm)	2σ	Mg#	δ^7Li(‰)-corr.
PL1202-3	Lherzolite	Olivine	8	7.28	2.07	1.56	0.29	90.1	6.86
		Opx	10	1.11	2.34	2.46	1.37	90.3	-
		Cpx	7	-3.23	1.29	6.28	3.07	91.5	-
PL1206-7	Lherzolite	Olivine	8	6.64	1.91	2.06	0.26	90.3	6.62
		Opx	10	1.03	2.25	1.90	0.86	90.4	-
		Cpx	4	-5.93	0.96	4.89	1.22	91.3	-
PL1301-J	Harzburgite	Olivine	8	7.29	1.99	1.50	0.27	90.5	7.51
		Opx	8	-0.71	2.45	0.95	0.17	91.0	-
		Cpx	3	-3.79	1.41	1.59	0.56	93.5	-
DB1302-D	Harzburgite	Olivine	10	8.99	2.04	1.13	0.22	91.0	8.45
		Opx	9	-0.92	2.38	1.49	0.21	91.2	-
		Cpx	5	-5.59	0.81	5.37	1.05	93.6	
PL1209-5	Harzburgite	Olivine	8	6.62	2.02	1.13	0.14	91.0	6.11
		Opx	8	-1.73	2.30	1.58	0.68	91.5	-
		Cpx	5	-4.89	0.92	6.23	1.36	94	-
PL14D3	Dunite	Olivine	8	6.62	1.94	1.91	0.12	90.7	7.0
PL14G3	Dunite	Olivine	8	5.60	2.09	1.29	0.15	91.8	5.86
#06JY31	Standard	Olivine		2.7	0.6	4.51	0.34	90.3	-
		Opx		1.33	0.24	-0.19	0.2	90.8	-
		Cpx		1.16	0.02	-2.37	0.44	91.1	-
#06JY34	Standard	Olivine		1.46	0.08	3.33	0.16	91.5	-

Opx: orthopyroxene; Cpx: clinopyroxene; Mg#= $100*Mg^{2+}/(Mg^{2+}+Fe^{2+})$; N: number of analysis;
SE: uncertainty (standard error) of measurements; σ: standard deviation of the mean;
#: Mineral standards used in the analysis from Su et al. (2015a).

Table A7 Li elemental and isotopic compositions of minerals in the Purang peridotites.

Sample	Point	Grains	Comment	δ^7Li (corr.)	1SE	Li(ppm)	1SE
PL1202-2	OL@1	G-1	coarse	6.63	0.28	1.79	0.01
	OL@2	G-2	coarse	6.93	1.13	1.33	0.01
	OL@3	G-3	coarse	6.69	1.00	1.51	0.01
	OL@4	G-4	coarse	6.52	1.00	1.64	0.01
	OL@5	G-5	coarse	6.30	0.97	1.51	0.01
	OL@6	G-6	coarse	7.82	1.00	1.68	0.01
	OL@7	G-7	coarse	8.54	1.00	1.51	0.01
	OL@8	G-8	coarse	8.79	1.17	1.47	0.01
	OPX@1	G-1	coarse	1.18	1.12	3.49	0.02
	OPX@2	G-1	coarse	-0.01	1.18	1.81	0.01
	OPX@3	G-2	rim	1.15	1.09	1.81	0.01
	OPX@4	G-2	core	1.28	1.12	2.93	0.02
	OPX@5	G-2	core	-0.20	1.10	2.35	0.01
	OPX@6	G-2	core	1.68	1.26	2.43	0.02
	OPX@7	G-2	rim	0.92	1.33	3.65	0.06
	OPX@8	G-2	core	2.40	1.11	1.81	0.01
	OPX@9	G-3	coarse	-0.28	1.18	2.01	0.01
	OPX@10	G-4	fine	2.97	1.20	2.27	0.01
	CPX@1	G-1	coarse	-3.26	0.57	7.00	0.02
	CPX@2	G-1	coarse	-5.06	0.73	7.18	0.05
	CPX@3	G-2	fine	-4.86	0.44	4.01	0.01
	CPX@4	G-2	fine	0.12	0.56	4.34	0.05
	CPX@5	G-3	coarse	-3.39	0.89	6.10	0.03
	CPX@6	G-3	coarse	-4.77	0.63	7.83	0.08
	CPX@7	G-3	coarse	-1.41	0.70	7.49	0.03
PL1206-7	OL@1	G-1	fine	5.88	0.97	2.15	0.01
	OL@2	G-2	fine	7.01	1.00	1.85	0.01
	OL@3	G-3	fine	5.78	0.93	2.15	0.01
	OL@4	G-4	fine	6.08	0.92	2.23	0.01
	OL@5	G-5	fine	7.88	0.97	1.97	0.02
	OL@6	G-6	fine	7.11	0.98	1.94	0.02
	OL@7	G-7	fine	7.34	0.98	2.04	0.01
	OL@8	G-8	fine	6.07	0.90	2.15	0.02
	OPX@1	G-1	fine	1.76	1.10	1.46	0.01
	OPX@2	G-1	fine	1.18	1.15	1.65	0.01
	OPX@3	G-2	coarse	-2.24	1.05	2.93	0.02
	OPX@4	G-3	rim	3.27	1.13	1.48	0.01
	OPX@5	G-3	mantle	1.73	1.14	1.79	0.01
	OPX@6	G-3	mantle	2.07	1.11	2.13	0.01
	OPX@7	G-3	core	0.57	1.12	1.70	0.01
	OPX@8	G-3	core	1.45	1.16	1.81	0.01
	OPX@9	G-3	core	0.90	1.23	2.15	0.02
	OPX@10	G-3	rim	-0.41	1.07	1.87	0.01
	CPX@1	G-1	fine	-5.02	0.44	4.48	0.02
	CPX@2	G-1	fine	-4.29	0.58	4.36	0.01
	CPX@3	G-1	fine	-6.90	0.45	5.03	0.02
	CPX@4	G-1	fine	-7.54	0.45	5.70	0.02
PL1301-J	OL@1	G-1	coarse	7.20	1.01	1.54	0.01
	OL@2	G-2	coarse	7.42	0.98	1.67	0.01
	OL@3	G-3	coarse	9.07	1.05	1.66	0.01
	OL@4	G-4	coarse	6.82	0.96	1.38	0.01
	OL@5	G-5	coarse	6.76	0.98	1.33	0.01

	OL@7	G-5	coarse	8.90	1.01	1.34	0.01
	OL@8	G-5	coarse	6.16	0.93	1.54	0.01
	OL@6	G-6	coarse	6.03	1.02	1.52	0.01
	OPX@1	G-1	rim	0.30	1.27	0.85	0.01
	OPX@2	G-1	mantle	-1.65	1.23	1.02	0.01
	OPX@3	G-1	core	-0.76	1.21	1.00	0.01
	OPX@4	G-1	core	-1.95	1.15	1.05	0.01
	OPX@5	G-1	core	-2.01	1.21	1.01	0.01
	OPX@6	G-1	rim	-0.22	1.19	0.96	0.01
	OPX@7	G-2	fine	1.07	1.28	0.89	0.01
	OPX@8	G-2	fine	-0.47	1.29	0.82	0.01
	CPX@1	G-1	fine	-4.09	0.73	1.29	0.01
	CPX@2	G-1	fine	-5.22	0.67	1.84	0.01
	CPX@3	G-1	fine	-2.06	0.72	1.63	0.01
DB1302-D	OL@1	G-1	fine	8.31	1.04	1.24	0.01
	OL@2	G-2	fine	10.18	0.98	1.15	0.01
	OL@3	G-3	fine	10.38	0.99	1.09	0.01
	OL@4	G-3	fine	9.34	0.98	1.15	0.01
	OL@5	G-3	fine	8.06	1.08	0.93	0.01
	OL@6	G-4	mantle	8.09	0.97	1.34	0.01
	OL@7	G-4	core	8.63	0.94	1.04	0.01
	OL@8	G-4	core	8.01	1.09	1.08	0.01
	OL@9	G-4	mantle	9.69	1.07	1.07	0.01
	OL@10	G-4	rim	9.16	1.07	1.16	0.01
	OPX@1	G-1	rim	-1.86	1.14	1.56	0.01
	OPX@2	G-1	mantle	-0.89	1.14	1.50	0.01
	OPX@3	G-1	core	-1.34	1.21	1.38	0.01
	OPX@4	G-1	core	-0.57	1.20	1.63	0.01
	OPX@5	G-1	mantle	-1.29	1.35	1.64	0.01
	OPX@6	G-1	rim	0.57	1.17	1.43	0.01
	OPX@7	G-2	coarse	-0.71	1.15	1.47	0.01
	OPX@8	G-2	coarse	-2.32	1.15	1.43	0.01
	OPX@9	G-3	fine	0.07	1.20	1.34	0.01
	CPX@1	G-1	fine	-4.77	0.46	5.09	0.03
	CPX@2	G-1	fine	-5.85	0.41	4.85	0.00
	CPX@5	G-3	fine	-4.97	0.36	6.17	0.03
	CPX@6	G-3	fine	-6.57	0.42	5.13	0.02
	CPX@7	G-3	fine	-5.81	0.38	5.62	0.03
PL1209-5	OL@1	G-1	coarse	7.94	1.04	1.22	0.01
	OL@2	G-1	coarse	10.69	0.96	1.13	0.01
	OL@3	G-1	coarse	7.56	0.99	1.14	0.01
	OL@4	G-2	coarse	5.65	1.01	1.21	0.01
	OL@5	G-2	coarse	6.11	1.02	1.14	0.01
	OL@6	G-3	coarse	6.75	1.03	0.98	0.01
	OL@7	G-3	coarse	3.19	1.01	1.13	0.01
	OL@8	G-3	coarse	5.03	1.00	1.09	0.01
	OPX@1	G-1	mantle	-2.77	1.11	1.90	0.01
	OPX@2	G-1	core	-1.66	1.15	1.79	0.01
	OPX@3	G-1	core	-3.04	1.16	1.87	0.01
	OPX@4	G-1	rim	-3.48	1.11	1.86	0.01
	OPX@5	G-2	fine	-4.29	1.16	1.57	0.01
	OPX@6	G-3	coarse	1.47	1.16	1.50	0.01
	OPX@7	G-4	coarse	1.26	1.17	1.11	0.00
	OPX@8	G-4	coarse	-1.37	1.19	1.06	0.01
	CPX@1	G-1	fine	-2.13	0.41	5.97	0.02

	CPX@2	G-1	fine	-4.02	0.49	5.72	0.03
	CPX@3	G-2	fine	-5.16	0.54	7.26	0.06
	CPX@4	G-3	fine	-6.78	0.43	5.63	0.03
	CPX@5	G-4	fine	-6.37	0.43	6.55	0.03
PL14D3	OL@1	G-1	coarse	6.32	0.99	1.94	0.01
	OL@2	G-2	coarse	6.17	0.97	1.86	0.01
	OL@3	G-3	coarse	7.93	0.91	1.91	0.01
	OL@4	G-4	coarse	6.20	0.99	2.01	0.01
	OL@5	G-5	coarse	7.08	0.96	1.96	0.01
	OL@6	G-6	coarse	5.03	1.01	1.90	0.01
	OL@7	G-7	coarse	7.39	0.93	1.82	0.01
	OL@8	G-8	coarse	6.87	0.99	1.91	0.01
PL14G3	OL@1	G-1	coarse	6.40	1.07	1.19	0.01
	OL@2	G-2	coarse	5.98	0.94	1.37	0.01
	OL@3	G-3	coarse	7.46	0.95	1.35	0.01
	OL@4	G-4	core	4.96	1.51	1.19	0.01
	OL@5	G-4	core	5.62	0.96	1.28	0.01
	OL@6	G-4	core	7.23	1.02	1.24	0.01
	OL@7	G-4	rim	2.76	0.97	1.37	0.01
	OL@8	G-5	coarse	4.44	0.93	1.30	0.01

Ol: olivine; Opx: orthopyroxene; Cpx: clinopyroxene
SE: uncertainty (standard error) of measurements;

References Cited:

Bao, P.S., Su, L., Wang, J., and Zhai, Q.G., 2013, Study on the tectonic setting for the ophiolites in Xigaze, Tibet: Acta Geologica Sinica, v. 87, p. 395–425.

Cheng, C., Zheng, H., Kapsiotis, A., Liu, W.L., Lenaz, D., Velicogna, M., Zhong, L.F., Huang, Q.T., Yuan, Y.J., and Xia, B., 2018, Geochemistry and geochronology of dolerite dykes from the Daba and Dongbo peridotite massifs, SW Tibet: Insights into the style of mantle melting at the onset of Neo-Tethyan subduction: Lithos, v. 322, p. 281–295.

Chu, Z.Y., Yan, Y., Chen, Z., Guo, J.H., Yang, Y.H., Li, C.F., and Zhang, Y.B., 2015, A comprehensive method for precise determination of Re, Os, Ir, Ru, Pt, Pd concentrations and Os isotopic compositions in geological samples: Geostandards and Geoanalytical Research, v. 39, p. 151–169.

Dai, J.G., Wang, C.S., Polat, A., Santosh, M., Li, Y.L., and Ge, Y.K., 2013, Rapid forearc spreading between 130 and 120 Ma: evidence from geochronology and geochemistry of the Xigaze ophiolite, southern Tibet: Lithos, v. 172-173, p. 1–16.

Dubois-Coté, V., Hébert, R., Dupuis, C., Wang, C.S., Li, Y.L., and Dostal, J., 2005, Petrological and geochemical evidence for the origin of the Yarlung Zangbo ophiolites, southern Tibet: Chemical Geology, v. 214, p. 265–286.

Gale, A., Dalton, C.A., Langmuir, C.H., Su, Y., and Schilling, J.G., 2013, The mean composition of ocean ridge basalts: Geochemistry, Geophysics, Geosystems, v. 14, p. 489–518.

Gao, Y., Snow, J.E., Casey, J.F., and Yu, J., 2011, Cooling-induced fractionation of mantle Li isotopes from the ultraslow-spreading Gakkel Ridge: Earth and Planetary Science Letters, v. 301, p. 231–240.

Gong, X.H., Shi, R.D., Griffin, W.L., Huang, Q.S., Xiong, Q., Chen, S.S., Zhang, M., and O'Reilly, S. Y., 2016. Recycling of ancient subduction-modified mantle domains in the Purang ophiolite (southwestern Tibet): Lithos, v. 262, p. 11–26.

Gong, X.H., Shi, R.D., Xu, J.F., Huang, Q.S., Huang, X.X., Su, B.X., 2020. “Garnet” Lherzolites in the Purang Ophiolite, Tibet: Evidence for Exhumation of Deep Oceanic Lithospheric Mantle: Geophysical Research Letters v. 47, p. e2019GL086101.

Huang, X.X., Sun, Y.L., Zhao, S.Q., and Yue, Y.H., 2018, Determination of Re by isotope dilution multi-collector inductively coupled plasma-mass spectrometry combined with a new extraction

chromatographic method for separation of Re in geological samples: Analytical Letters, v. 51, p. 1122–1146.
Ishizuka, O., Tani, K., Reagan, M.K., Kanayama, K., Umino, S., Harigane, Y., Sakamoto, I., Miyajima, Y., Yuasa, M., and Dunkley, D.J., 2011, The timescales of subduction initiation and subsequent evolution of an oceanic island arc: Earth and Planetary Science Letters, v. 306, p. 229–240.
Li, J., Zhao, P.P., Liu, J.G., Wang, X.C., Yang, A.Y., Wang, G.Q., Xu, J.F., 2015. Reassessment of hydrofluoric acid desilicification in the Carius tube digestion technique for Re-Os Isotopic determination in geological samples: Geostandards and Geoanalytical Research, v. 39, p. 17–30.
Liu, F., Yang, J.S., Chen, S.Y., Li, Z.L., Lian, D.Y., Zhou, W.D., Zhao, W., 2013. Geochemistry and Sr-Nd-Pb isotopic composition of mafic rocks in the western part of Yarlung Zangbo suture zone: Evidence for intra-oceanic supra-subduction within the Neo-Tethys: Geology in China, v. 40, p. 361–374 (in Chinese with English abstract).
Liu, F., Yang, J.S., Lian, D.Y., Zhao, H., Zhang, L., and Huang, J., 2015a, Geogenesis and characteristics of the western part of the Yarlung Zangbo ophiolites, Tibet: Acta Petrologica Sinica, v. 31, p. 3609–3628 (in Chinese with English abstract).
Liu, F., Yang, J.S., Lian, D.Y., Zhao, H., Zhao, Y.J., and Zhang, L., 2015b, Geogenesis and tectonic significance of mafic dikes in the western part of the Yarlung Zangbo suture zone, Tibet: Acta Geoscientica Sinica, v. 36, p. 443–456 (in Chinese with English abstract).
Liu, F., Dilek, Y., Xie, Y., Yang, J., and Lian, D., 2018a, Melt evolution of upper mantle peridotites and mafic dikes in the northern ophiolite belt of the western Yarlung Zangbo suture zone (southern Tibet): Lithosphere, v. 10.
Liu, F., Lian, D.Y., Niu, X.L., Zhao, H., Feng, G.Y., and Yang, J.S., 2018b, Dongbo MORB-Type isotropic gabbro emplaced as an oceanic core complex in Western Yarlung Zangbo Suture Zone, Tibet: Earth Science, v. 43, p. 952–974 (in Chinese with English abstract).
Liu, Z., Li, Y., Xiong, F.H., Wu, D., and Liu, F., 2011, Petrology and geochronology of MOR gabbro in the Purang ophiolite of western Tibet, China: Acta Petrologica Sinica, v. 27, p. 3269–3279 (in Chinese with English abstract).
Macleod, C.J., Lissenberg, J.C., and Bibby, L.E., 2013, "Moist MORB" axial magmatism in the Oman ophiolite: the evidence against a mid-ocean ridge origin: Geology, v. 41, p. 459–462.
Meisel, T., Walker, R.J., Irving, A.J., Lorand, J.P. 2001. Osmium isotopic composition of mantle xenoliths: a global perspective: Geochimica et Cosmochimica Acta, v. 65, p. 1311–1323.
Miller, C., Schuster, R., Thöni, M., Frank, W., and Meisel, T., 2003, Geochemistry and tectonomagmatic affinity of the Yungbwa ophiolite, SW Tibet: Lithos, v. 66, p. 155–172.
Miyashiro, A., 1974, Volcanic rock series in island arcs and active continental margins. American Journal of Sciences, v. 257, p. 609–647.
Pearce, J.A., 1982, Trace element characteristics of lavas from destructive plate boundaries. In: Thorpe, R.S. (Ed.), Orogenic Andesites. Wiley, Chichester, U.K. 528–548.
Pearce, J. A., 2014, Immobile element fingerprinting of ophiolites: Elements, v. 10, p. 101–108.
Reagan, M.K., Ishizuka, O., Stern, R.J., Kelley, K.A., Ohara, Y., Blichert-Toft, J., Bloomer, S.H., Cash, J., Fryer, P., Hanan, B.B., Hickey-Vargas, R., Ishii, T., Kimura, J.I., Peate, D.W., Rowe, M.C., and Woods, M., 2010, Fore-arc basalts and subduction initiation in the Izu-Bonin-Mariana system: Geochemistry, Geophysics, Geosystems, v. 11, Q03X12.
Reagan, M.K., McClelland, W.C., Girard, G., Goff, K.R., Peate, D.W., Ohara, Y., and Stern, R.J., 2013, The geology of the southern Mariana fore-arc crust: implications for the scale of Eocene volcanism in the western Pacific: Earth and Planetary Science Letters, v. 380, p. 41–51.
Seitz, H.M., and Woodland, A.B., 2000, The distribution of lithium in peridotitic and pyroxenitic mantle lithologies: an indicator of magmatic and metasomatic processes: Chemical Geology, v. 166, p. 47–64.
Seitz, H.M., Brey, G.P., Lahaye, Y., Durali, S., and Weyer, S., 2004, Lithium isotopic signatures of peridotite xenoliths and isotopic fractionation at high temperature between olivine and pyroxenes: Chemical Geology, v. 212, p. 163–177.

Shervais, J.W., 1982, Ti-V plots and the petrogenesis of modern and ophiolitic lavas: Earth and Planetary Science Letters, v. 59, p. 110–118.

Shervais, J.W., Reagan, M., Haugen, E., Almeev, R.R., Pearce, J.A., and Prytulak, J., et al. 2019, Magmatic response to subduction initiation: Part 1. Fore-arc basalts of the Izu-Bonin arc from IODP Expedition 352: Geochemistry, Geophysics, Geosystems, v. 20, p. 314–338.

Taylor, R.N., Nesbitt, R.W., Vidal, P., Harmon, R.S., Auvray, B., and Croudace, I.W., 1994, Mineralogy, chemistry, and genesis of the Boninite Series Volcanics, Chichijima, Bonin Islands, Japan: Journal of Petrology, v. 35, p. 577–617.

Taylor, R.N., and Nesbitt, R.W., 1995, Arc volcanism in an extensional regime at the initiation of subduction: a geochemical study of Hahajima, Bonin Islands, Japan. In: Smellie, J. (Ed.), Volcanism associated with Extension at Consuming Plate Margins: Geological Society of London, Special Publications, v. 81, p. 115–134.

Xiong, F.H., Meng, Y.K., Yang, J.S., Liu, Z., Xu, X.Z., Eslami, A., and Zhang, R., 2020, Geochronology and petrogenesis of the mafic dykes from the Purang ophiolite: Implications for evolution of the western Yarlung-Tsangpo suture zone, southwestern Tibet: Geoscience Frontiers, v. 11, p. 277–292.

Yang, S.B., Li, Y., Yang, J.S., Li, R.B., Dong, T.C., and Pei, L., 2017, Baimarang ophiolite in Xigaze, Tibet: A small ocean basin close to the Asian continental margin: Acta Petrologica Sinica, v. 33(12), p. 3766–3782 (in Chinese with English abstract).

Zhang, L.L., Liu, C.Z., Wu, F.Y., Zhang, C., Ji, W.Q., and Wang, J.G., 2016, Sr–Nd–Hf isotopes of the intrusive rocks in the Cretaceous Xigaze ophiolite, southern Tibet: constraints on its formation setting: Lithos, v. 258–259, p. 133–148.

Zheng, H., Huang, Q., Kapsiotis, A., Xia, B., Yin, Z., Zhong, Y., Lu, Y., and Shi, X., 2017, Early Cretaceous ophiolites of the Yarlung Zangbo suture zone: Insights from dolerites and peridotites from the Baer upper mantle suite, SW Tibet (China): International Geology Review, v. 59, p. 1471–1489.

Zheng, H., Huang, Q., Kapsiotis, A., Lenaz, D., Velicogna, M., Xu, C., Cheng, C., Xia, B., Liu, W., Xiao, Y., and Yang, P., 2019, Coexistence of MORB- and OIB-like dolerite intrusions in the Purang ultramafic massif, SW Tibet: A paradigm of plume-influenced MOR-type magmatism prior to subduction initiation in the Neo-Tethyan lithospheric mantle: Geological Society of America Bulletin, v. 131, p. 1276–1294.